Available online at www.sciencedirect.com
ScienceDirect
Trans. Nonferrous Met. Soc. China 30(2020) 2775−2791
Transactions of Nonferrous Metals Society of China
www.tnmsc.cn

Instantaneous and long-term deformation characteristics of deep room-pillar system induced by pillar recovery

Xi-bing LI[1], Jia-dong QIU[1,2], Yu-zhe ZHAO[1], Zheng-hong CHEN[1], Di-yuan LI[1]

1. School of Resources and Safety Engineering, Central South University, Changsha 410083, China;
2. Shenzhen Key Laboratory of Deep Underground Engineering Sciences and Green Energy, Shenzhen University, Shenzhen 518060, China

Received 17 February 2020; accepted 4 August 2020

Abstract: The goaf may face a series of deformation and settlement problems when the room-pillar mining method is used to excavate ore and pillars in the deep strata. To this end, a deep room-pillar model with two levels was made, and the pillar recovery was carried out. The instantaneous deformation responses during the pillars recovery and the long-term settlements after the pillar recovery were analyzed. During the pillar recovery, different regions of surrounding rocks suffer from different dynamic disturbances which can be divided into three types, including (I) the combined action of blasting disturbance and unloading disturbance, (II) the sequential action of blasting disturbance and unloading disturbance, and (III) the action of unloading disturbance. After the pillar recovery, the settlement above the first recovering pillar is the largest, which has a traction effect on the settlement in other areas. The settlement process can be divided into two stages, stable displacement stage and unstable displacement stage. When the pillar-room system undergoes the unstable displacement stage, rock spalling and further cascading collapse will occur.

Key words: room-pillar system; physical model test; settlement; dynamic response; deformation

1 Introduction

Pillars are usually designed to support the overburden to ensure personnel and equipment safety [1,2]. With the massive development of mineral resources, more and more mines are considering recovering the pillars to supplement the ore production and improve the economic benefits [3−5]. When the pillar is mined, the deformation and stress redistribution usually occur in the surrounding rock, and even the adjacent structures may be unstable. Therefore, it is necessary to analyze the influence of the pillar recovery on the stability of the room-pillar system.

In past decades, the stability evaluation of the pillars has attracted a lot of attention [6−8]. For example, the tributary area method, which has been widely applied to the estimation of average pillar stress, was developed by assuming that the individual pillar can bear the full load of the overlying strata and half of overburden of the adjacent tunnel [9,10]. The pressure arch method was proposed for calculating the coal pillar load [11], and used to evaluate the settlement risk of a coal mine in Australia [12]. ESTERHUIZEN et al [13] further considered the potential impact of failed pillars and proposed a pillar strength assessment method. LUNDER and PAKALNIS [14] combined the tributary area method and boundary element analysis to provide a more rigorous method for the pillar strength evaluation. In fact, the deformation and failure behaviors of the room-pillar system are more complex and unpredictable than those of the pillars. In order to facilitate the design and stability evaluation of

---

Foundation item: Projects (11972378, 41630642) supported by the National Natural Science Foundation of China
Corresponding author: Jia-dong QIU; E-mail: jdq1991@csu.edu.cn
DOI: 10.1016/S1003-6326(20)65420-6

pillars, some scholars have defined the safety index, which can be calculated as the ratio of pillar strength to the average stress [13]. However, ESTERHUIZEN et al [13] found that even if some pillars have high safety indexes, they will still fail without any portent.

A great deal of effort has been devoted to understand the bearing and failure characteristics of pillars or room-pillar systems. For example, ZHOU et al [15,16] and ZHU et al [17] carried out a series of experiments and simulations to study the effects of mining activities on the deformation, failure and stress redistribution characteristics of the room-pillar systems. FANG and HARRISON [18] developed a local degradation model for analyzing the progressive failure characteristics of pillars. Using the numerical simulation and empirical methods, ALHEIB et al [19] also analyzed the cascading pillar collapse phenomenon of a chalk mine in Paris. In fact, it is very difficult to accurately evaluate the stability of the room-pillar systems. Some scholars have found that when the mining activities are carried out in lower strata, it is easy to induce the progressive failure and subsidence of the pillar and roof in upper strata [17,20,21]. However, in some special environments, the transfer of overburden of failed pillar causes the adjacent supporting structure to be overloaded, which may further lead to the large-scale cascading failure of the room-pillar system [22,23].

Most of the previous studies of stability evaluation of the pillars or room-pillar system were based on the static theory. However, during the mining process, the surrounding rock is not only subjected to the blasting stress wave, but also transfers the load under the effect of accompanying dynamic disturbance [24−26]. At present, only a few studies have paid attention to the influence of the accompanying dynamic disturbance on the mechanical behavior of the pillars or room-pillar system [16,27]. For example, LI et al [28] studied the dynamic response characteristics of the single pillar under high stress, and found that with the increase of the initial static stress, even a small dynamic disturbance will cause the plastic failure. ZHOU et al [16] analyzed the dynamic response characteristics of the room-pillar system during pillar recovery, and concluded that the calculation of load transfer only considering the static loading conditions is not rigorous and the load transfer of adjacent pillar is underestimated. At the same time, they also showed that some goafs which are stable under the static analysis may also be failed under the dynamic analysis. Although previous studies provided important insights into the mechanical behavior of the room-pillar system, these studies tended to analyze the case of shallow strata, and rarely considered the case in the deep strata. Especially, the research based on the combination of static and dynamic loading was less. Therefore, it is necessary to carry out the dynamic study of a deep room-pillar system.

In this study, a room-pillar system with two levels was made using similar materials. The influence of lower level pillar recovery on the upper level was studied. Using the digital image correlation (DIC) system, the instantaneous deformation response characteristics during the pillar recovery were analyzed, and the long-term settlement characteristics after the pillar recovery were investigated.

2 Description of Linglong Gold Mine

In the present study, the mining situation of Linglong Gold Mine, Shandong Province, China, was used as a prototype. In Linglong Gold Mine, there are two main mining methods used for ore mining, namely the room-pillar mining method and the backfill mining method. For the vein with a thickness less than or equal to 6 m, the room-pillar mining method is usually adopted, while for the vein with a thickness greater than 6 m, the backfill mining method is used. The pillars are often mined by the centralized hole arrangement and one-time blasting during the room-pillar mining. However, only the high-grade pillars are mined while the low-grade pillars are often remaining during the backfill mining. After the pillar recovery, the backfill mining method usually carries out the cemented filling treatment in the original area, while the room-pillar method does not. At present, in Linglong Gold Mine, the adoption ratio of the room-pillar method to the backfill mining method is about 3:7. Regardless of the mining methods, multiple levels are often mined simultaneously. Moreover, the mining environment is becoming more and more complex with the increase of mining depth. Especially in the area without filling treatment, the risk of roof subsidence and collapse will increase dramatically. Therefore, the Linglong Gold Mine is also actively studying the problems that these mining methods (especially the room-pillar mining method) may face in deep mining.

The in-situ stress condition of Linglong Gold Mine at different depths can be given by the fitting equations as follows [29]:

$$\sigma_{\mathrm{hmax}}=0.4612+0.0588h \tag{1}$$

$$\sigma_{\mathrm{hmin}}=-0.4346+0.0286h \tag{2}$$

$$\sigma_{\mathrm{v}}=-0.4683+0.0316h \tag{3}$$

where σ_{hmax}, σ_{hmin} and σ_{v} are the maximum horizontal principal stress, minimum horizontal principal stress and vertical principal stress, respectively; h is the buried depth.

3 Description of physical model test

3.1 Experimental system

In this study, the test system consists of servo loading devices and digital image correlation (DIC) system, as shown in Fig. 1. The servo loading devices are composed of horizontal hydraulic jacks, vertical hydraulic jacks, indenters, hydraulic pump and control instruments (the hydrolic pump and control instruments are not shown in Fig. 1). The control instruments send out action instructions to the hydraulic pump and control the whole loading system. Uniform vertical stress and horizontal stress can be applied through hydraulic jacks and indenters.

The DIC method is a non-contact optical technique for deformation measurement [30−32]. By tracking the spatial positions of the same marked points in two images, the displacement, strain and velocity information of model surfaces can be calculated. The DIC system consists of two high-speed cameras, one static camera, four light sources, and one data analyzing system, as shown in Fig. 1. The static camera is 3.6 m away from the physical model, and the high-speed cameras are 8.5 m away from the physical model. On the front surface of the physical model, a series of marked points were made with white matte paint, and the diameters of the marked points are 3−5 mm. The deformation acquisition process based on the DIC system can be divided into two stages: (1) the deformation acquisition phase during pillar recovery; (2) the deformation acquisition phase after pillar recovery. In the first stage, the high-speed cameras are used to collect the surface

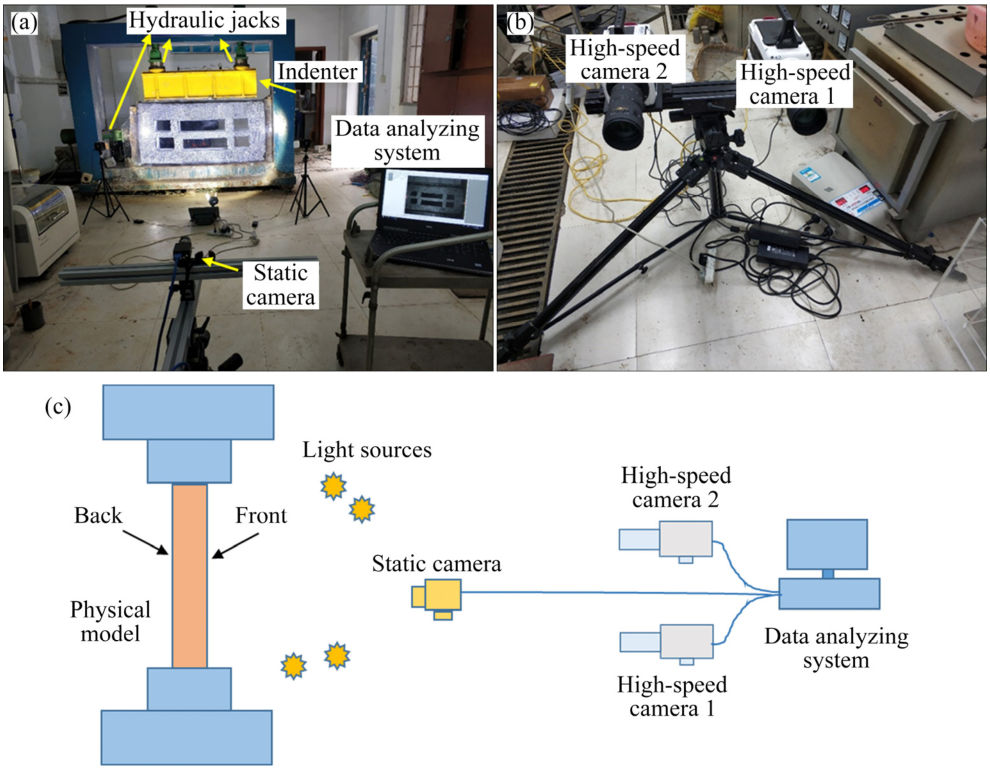

Fig. 1 Experimental system of physical model: (a) Loading device and static camera; (b) High cameras; (c) Schematic diagram of digital image correlation technique

deformation of the physical model during the pillar recovery, and the resolution of high-speed cameras is set to be 320 × 240 pixels. In the second stage, the high-speed cameras are stopped, then the static camera with a resolution of 4096 × 3000 pixels is used to collect the long-term deformation characteristics of the physical model after the pillar recovery.

3.2 Physical model design

In this study, the room-pillar mining method was adopted. In the prototype design of Linglong Gold Mine, the length of the ore room is generally 30−60 m and the length of the pillar is 3−6 m. Therefore, the real dimensions of the Linglong Gold Mine were considered as room length of 36 m, pillar size of 3 m × 4.5 m (width × height), roof thickness of 3 m, and the maximum vein thickness of 6 m. However, it is meaningless and impossible to make a test model in real dimension; thus, using similar materials, a physical model with scaled dimensions was made by considering the similarity constants. According to the engineering conditions and the loading condition of the servo loading devices, the similarity constant of geometry K_L and the similarity constant of density K_ρ were determined to be K_L=30 and K_ρ=1.4. Based on the similar criteria [33,34], other similarity constants can be further derived: $K_\sigma=K_{\sigma c}=K_E=K_LK_\rho=42$, and $K_\varepsilon= K_\mu=1$ (K_σ, $K_{\sigma c}$, K_E, K_ε and K_μ are the similarity constants for stress, strength, elastic modulus, strain and Poisson ratio, respectively). The similar materials consist of quartz sand, iron powder, cement, alpha hemihydrate gypsum, water reducer, gypsum retarder and water. The mix ratio of quartz sand, iron powder, gypsum, cement, gypsum retarder, water reducer, and water is 16:4:4:1:0.082:0.15:4.165 (mass ratio). For the quartz sand, three particle sizes (850−355, 355−200 and 355−125 μm) with the mix ratio of 1:1:1 were used. The mechanical parameters of the granite in Linglong Gold Mine and the similar material in physical model are shown in Table 1. According to Table 1, the similarity constant of P-wave velocity K_c is about 3.5. The similarity constant of time can be determined: $K_t= K_L/K_c$=8.6.

The dimensions of the physical model are 1700 mm × 800 mm × 200 mm. A total of 6 goafs were reserved and 8 pillars were prepared (Fig. 2(a)). As shown in Fig. 2(a), Pillars 1−8 are labeled P1−P8, respectively. Pillars 1, 4, 5 and 8 were set as the boundary pillars. Pillars 2 and 3 were set as the normal pillars in the lower level, and Pillars 6 and 7 were set as the normal pillars in the upper level. According to the similarity constant of geometry, the size of normal pillars was 100 mm × 150 mm (width × height), and the height of the lower roof was 100 mm. For the convenience of description, 6 goafs were numbered. The lower three goafs were L1−L3, and the above three goafs were U1−U3. Four rubber plates with a thickness of 10 mm were laid at the boundaries of the physical model. According to our previous study [33], these rubber plates could effectively absorb the stress waves at the boundaries, thus the boundaries of physical model are actually quasi viscous boundaries. Since many mining activities in Linglong Gold Mine at present were carried out at a depth of 750 m, the deformation characteristics of the room-pillar system with a depth of 750 m were studied. In this study, it was assumed that the strike of ore vein was perpendicular to the direction of the maximum horizontal principal stress. According to Eqs. (2) and (3), the minimum horizontal principal stress σ_{hmin} and vertical principal stress σ_{v} were 21.02 and 23.23 MPa, respectively. Considering the similarity constant of stress K_σ, the horizontal and vertical principal stresses provided by the servo loading devices were 0.5 and 0.55 MPa, respectively. During the experiment, the horizontal and vertical loads were applied to the model at a loading rate of 0.2 kN/s until the set horizontal and vertical principal stresses were achieved. Then, the horizontal and vertical loads were maintained at a rate of 0.01 kN/s until the end of the tests.

3.3 Pillar recovery scheme

In engineering practice, pillars are recovered

Table 1 Mechanical properties of materials

Material	Density/ ($\mathrm{kg \cdot m^{-3}}$)	UCS strength/MPa	Elastic modulus/GPa	Poisson ratio	P-wave velocity/($\mathrm{m \cdot s^{-1}}$)
Granite in Linglong Gold Mine	2650−2740	137.7−163.8	21.4−63.7	0.23−0.26	5400−5695
Similar material	1930−1960	3.3−3.9	0.36−0.74	0.23−0.25	1540−1680

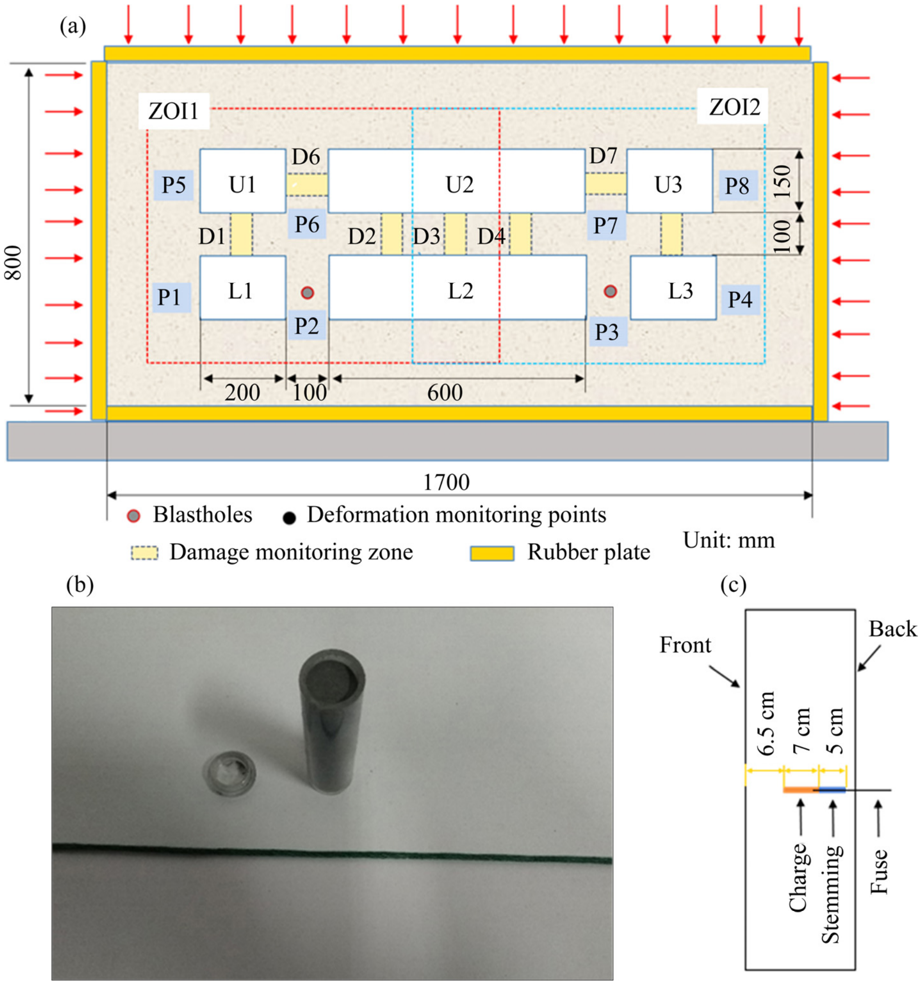

Fig. 2 Schematic diagram of physical model and blasting source setting: (a) Physical model; (b) Cylindrical charge; (c) Blasthole layout

by the centralized hole arrangement and one-time blasting. In this work, only the dynamic responses induced by the blasting without considering the specific blasthole arrangement were concerned, so the simplified blasting sources were made. By using the electric hammer, the blastholes with a diameter of 18 mm and a depth of 135 mm can be excavated. As shown in Fig. 2(a), two blastholes were excavated on Pillars 2 and 3. The cylindrical charge with a diameter of 17 mm and a length of 70 mm was prepared, as shown in Fig. 2(b). The cylindrical charge was mainly made by 9.4 g black powder and a plastic box with a thickness of 2 mm. The charge was embedded in the middle of the physical model and the blasthole was stemmed with the gypsum, as shown in Fig. 2(c). The pillar recovery scheme is as follows: Pillar 2 was first recovered by blasting, and then Pillar 3 was recovered after about 1 h. After the recovering work of the two pillars is completed, the boundary stresses of the physical model were kept unchanged, and the long-term deformation characteristics of the physical model were observed by the static camera.

4 Instantaneous deformation response and failure characteristics during pillar recovery

4.1 Deformation contour

Before the test, two interest zones (ZOI1 and ZOI2) with the dimensions of 700 mm × 500 mm were selected, as shown in Fig. 2(a). Correspondingly, high-speed camera 1 captures the images in ZOI1 and high-speed camera 2 captures the images in ZOI2. Pillars 2 and 3 are recovered by blasting, and the deformation response of the front surface of the physical model is shown in Figs. 3 and 4, respectively. The maximum principal strain (ε_1) was analyzed. In the DIC system, the tensile strain is positive and the compressive strain is

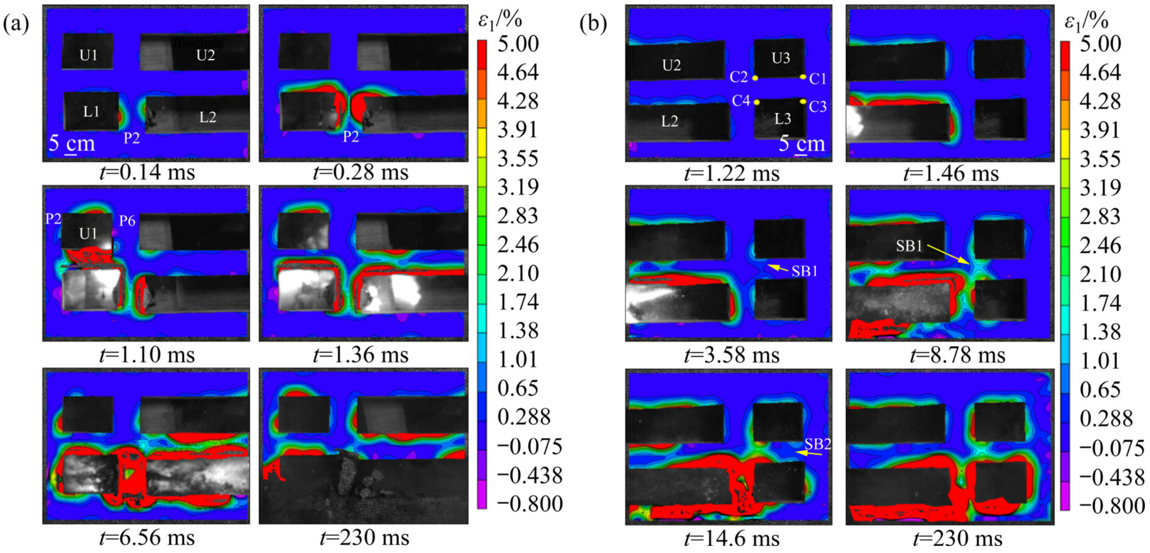

Fig. 3 Variation of maximum principal strain ε_1 during Pillar 2 recovery (P2—Pillar 2, P5—Pillar 5, P6—Pillar 6, SB—Strain growth band): (a) ZOI1; (b) ZOI2

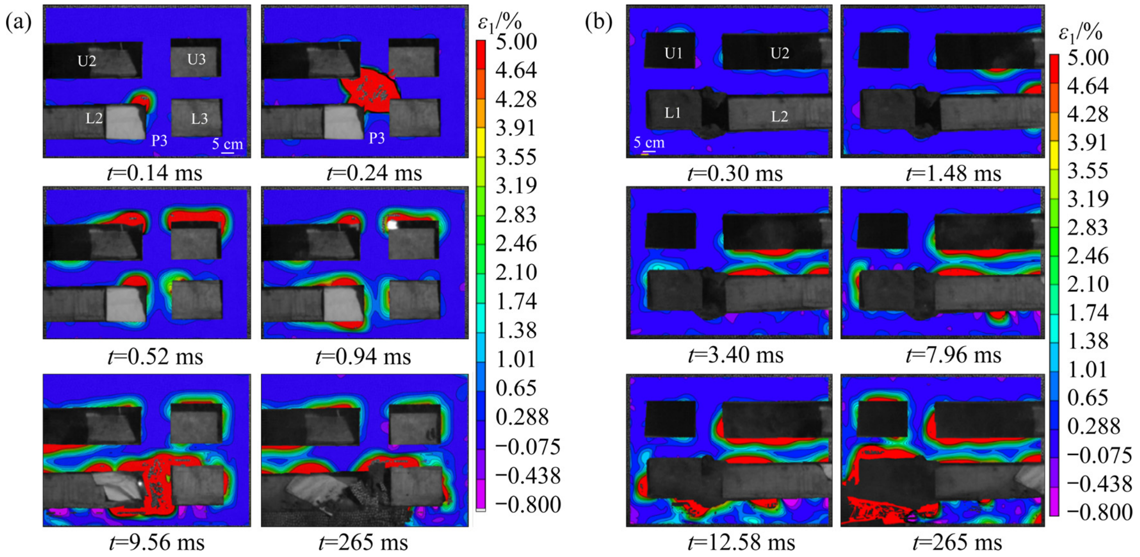

Fig. 4 Variation of maximum principal strain ε_1 during Pillar 3 recovery (P3—Pillar 3): (a) ZOI2; (b) ZOI1

negative. It should be noted that some dust and cracks generated by the blasting may cover or destroy the marker points, resulting in the fact that the strain at some points cannot be recognized. Once the strain cannot be recognized, the local contour will not be produced.

Figure 3 shows the contour of the maximum principal strain (ε_1) during Pillar 2 recovery. After the blasting starts, the strain first occurs near Pillar 2, as shown in the case of t=0.28 ms. Subsequently, the strain mainly propagates along the edges of the lower roof to the upper pillars and upper roofs. In addition, diffraction will occur when the strain propagates from the lower roofs to the upper roofs, which will cause the strain in the beginning and end regions of diffraction to be larger than that in the diffraction path region. For example, when t=1.10 ms, the diffraction start region and the diffraction end region are respectively below and above Goaf U1, and the diffraction path region is in Pillars 5 and 6. Obviously, the strains in the diffraction start region and the diffraction end region are larger than those in the diffraction path region. Moreover, it is easy to form the strain growth bands (SBs) between the corners of the upper goafs and the lower goafs. As shown in

Fig. 3(b), two strain growth bands SB1 and SB2 are formed between corners C1 and C3, C2 and C4, respectively. As the stress in the physical model is continuously adjusted from the left to the right, the strain on the right of Goaf L2 continues to increase, and further transfers to the upper part of Goaf U3 through strain growth bands SB1 and SB2. At t=230 ms, the surface strain of the physical model is basically stable.

Figure 4 shows the deformation contour of the model surface during Pillar 3 recovery. As shown in Fig. 4(a), shortly after the start of blasting (such as t=0.24 ms), a red strain concentration zone is formed above Pillar 3. Subsequently, the red strain concentration zones also appear above Goafs U2 and U3 with the diffraction of stress wave. At t=1.48 ms, the red strain zone extends into ZOI1, as shown in Fig. 4(b). Subsequently, the strain in ZOI1 gradually increases. At t=265 ms, the surface deformation of the model is basically stable.

4.2 Damage assessment of room-pillar system

Rock damage is an important index to assess the variation of the bearing capacity of rock mass [35−37]. In this section, the damage of the room-pillar system caused by pillar recovery is assessed. As shown in Fig. 2(a), five damage monitoring zones (D1−D5) were arranged in the lower roofs, and two damage monitoring zones (D6, D7) are arranged in the upper pillars. The damage index D is defined by the following equation:

$$D=\left[1-\left(v_{\mathrm{P}}/v_{\mathrm{P0}}\right)^2\right]\times 100\% \tag{4}$$

where v_{P} is P-wave velocity after pillar recovery, and v_{P0} is the initial P-wave velocity before pillar recovery.

Within 5 min before the pillar recovery, the P-wave velocities in the damage monitoring zones were measured by the ultrasonic testing device DB4C. Similarly, the P-wave velocities were also measured within 5 min after pillar recovery. Based on the results of the two P-wave tests, the damage index can be calculated by Eq. (4). Figure 5 presents the damage index of the lower roof and upper pillars before and after pillar recovery. The zero time is set to be the moment before the blasting of Pillar 2. As shown in Fig. 5, the damage index of the physical model increases gradually as the pillars are recovered in sequence. For the lower roof, the damage index is smaller than 10% after the pillar recovery. For the upper pillar, the damage index is smaller than 20% after the pillar recovery. Obviously, the damage of the upper pillar is greater than that of the lower roof.

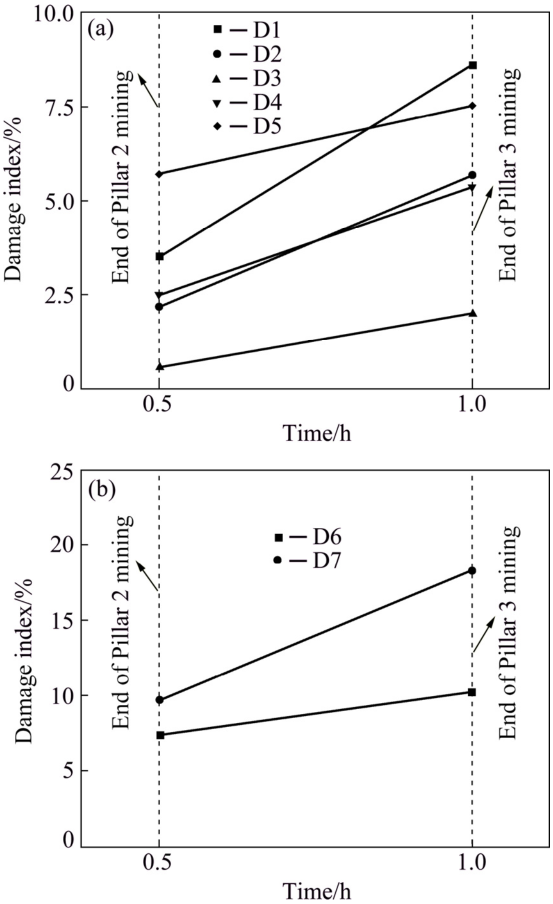

Fig. 5 Damage index of physical model before and after pillar recovery: (a) Lower roof; (b) Upper pillars

4.3 Rapid crack propagation induced by pillar recovery

In the process of pillar recovery, the overburden load originally acting on the recovered pillars will be quickly transferred to adjacent supporting structures [16], resulting in the stress concentration in adjacent structures and the unsafety of room-pillar system. Therefore, it is important to assess the stability of the room-pillar system before and after the pillar recovery. Figure 6 presents the process of the crack evolution of the physical model. In the process of Pillar 2 recovery, some small macroscopic cracks initiated quickly near the corners of Goaf U1, as shown in Fig. 6(a). In the process of Pillar 3 recovery, these small cracks were stimulated to further extend. In addition, some new cracks were generated at the corners of Goafs L1, U2, and U3. After the two pillars recovery, the room-pillar system is stable for a certain period of time.

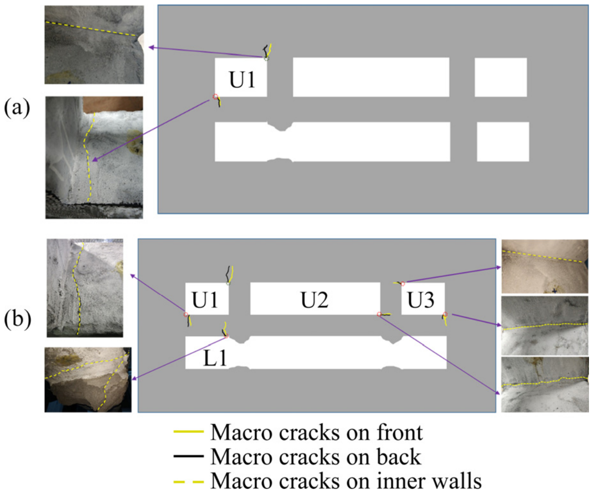

Fig. 6 Schematic diagram of crack propagation induced by pillar recovery: (a) Crack initiation induced by Pillar 2 recovery (t=0.05 h); (b) Crack initiation and propagation induced by Pillar 3 recovery (t=1 h)

The above-mentioned crack evolution process is mainly due to the redistribution of stress in the adjacent structure caused by pillar recovery. These crack evolutions occurred suddenly, indicating the transient response characteristics of the adjacent structures during the pillar recovery. In mining practice, although pillar recovery will cause damage to adjacent structures to a certain extent, the adjacent structures usually remain stable for a period of time. Similar to the engineering practice, the room-pillar system in this study is also stable for a period of time after the pillar recovery. However, due to the influence of in-situ stress, the adjacent structures usually creep and cause some settlement, which will gradually reduce the long-term stability of the adjacent structures and even induce some severer geological disasters [38−41]. Therefore, in the following sections, the long-term deformation characteristics of the room-pillar system will be analyzed.

5 Long-term deformation and failure characteristics under in-situ stress

5.1 Model settlement characteristics

In this section, the long-term deformation characteristics of the room-pillar system after the pillar recovery were analyzed. Figure 7 presents the contour of the vertical displacement with the associated deformation curves of the lower roof and upper roof (LF and UF) at typical times. At t=1 h, Pillar 3 recovery is finished. Under the long-term effect of the in-situ stress, the overall displacement near Pillar 6 is larger than that near Pillar 7, and the vertical displacements of the upper and lower zones of Pillar 6 are always the largest (as shown in Fig. 7). The displacement of the line LF is also larger than that of the line UF, which means that the displacement of the lower roof is larger than that of the upper roof. In addition, the difference of displacement between line LF and UF at t=1 h is small. However, with the increase of time, the displacement difference between LF and UF will gradually increase. Moreover, with the increase of the time, the settlement near Pillar 6 increases, which will further promote the bending of the roofs and the deformation of other areas. In general, the settlement of Pillar 6 plays a traction role in the deformation of other areas.

Figure 8 shows the relationship between the maximum vertical displacement of two lines LF and UF and time. As shown in Fig. 8, it can be found that the maximum displacement of lines LF and UF increases slowly at a small velocity before t=18 h, and the displacement increases significantly at a greater velocity after t=18 h. Overall, the settlement process of the room-pillar system can be divided into two stages, including the stable displacement stage and unstable displacement stage. In the stable displacement stage, the displacements of the room-pillar system increase approximately linearly with time, and the settlement velocity is generally small and stable. In the unstable displacement stage, since the crack propagation and local stress concentration in the model have reached to a certain degree, they will obviously stimulate the displacement increase and crack propagation in other regions. Therefore, in the unstable displacement stage, the displacement in the model will increase significantly, and the settlement velocity increases continuously.

5.2 Crack propagation and damage characteristics

Figure 9 shows the crack propagation process of the physical model under long-term in-situ stress. By comparing Fig. 6(b) with Fig. 9(a), it can be seen that three new macro cracks are added to the front and back surfaces of the physical model from 1 to 12 h. As shown in Fig. 9(b), from 12 to 18 h,

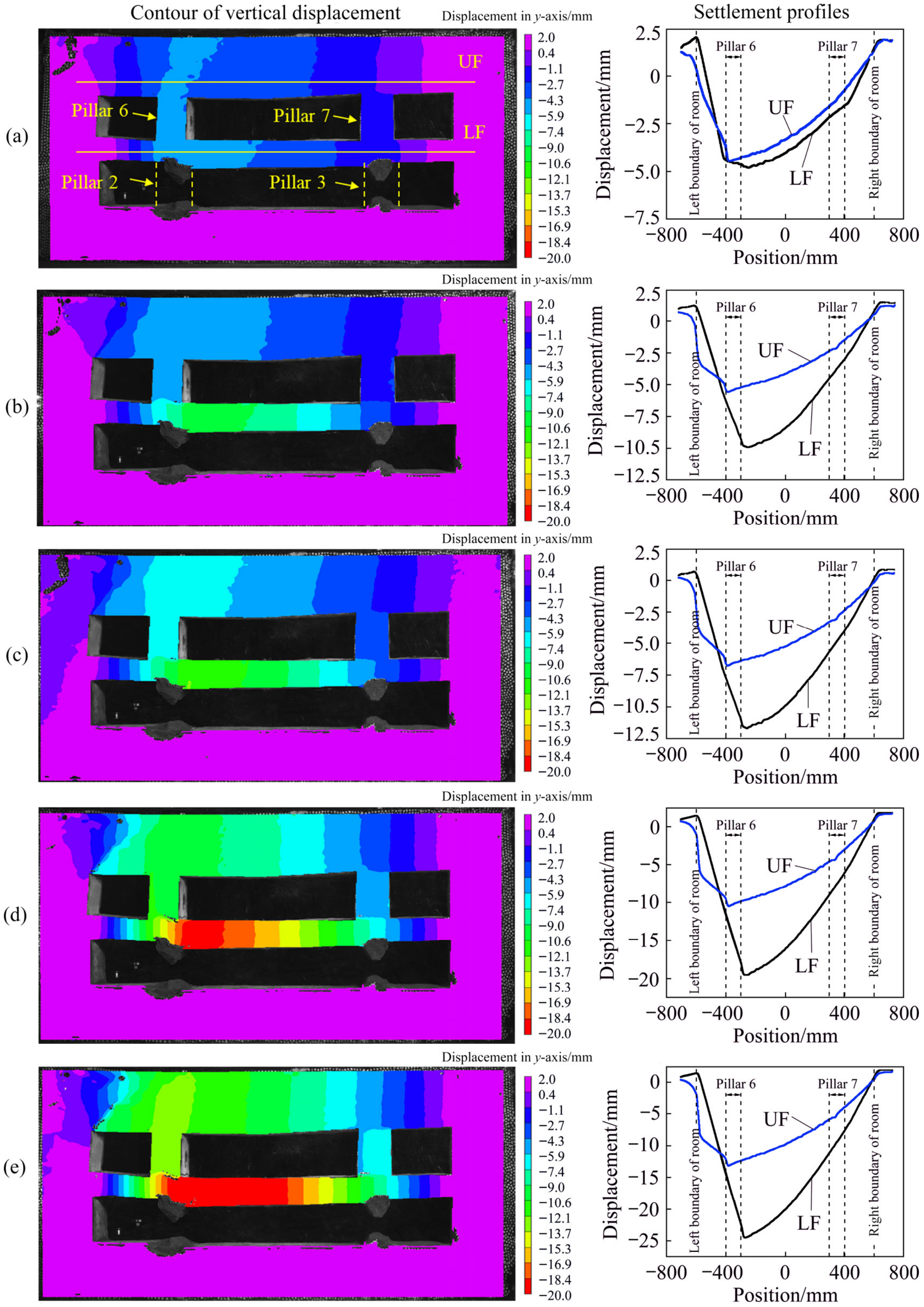

Fig. 7 Vertical displacement characteristics at typical time points under long-term in-situ stress: (a) t=1 h; (b) t=12 h; (c) t=18 h; (d) t=24 h; (e) t=27 h

the original macro cracks extend further, and some new cracks form below Pillar 6 and above Goaf U1. From 18 to 24 h, the damage above Goaf U1 increases significantly (see Fig. 9(c)). In particular, a new macro crack forms on the back surface of the physical model. Figure 9(d) shows that from 24 to 27 h, macro cracks extend continuously; moreover, there is obvious rock spalling on the back and top

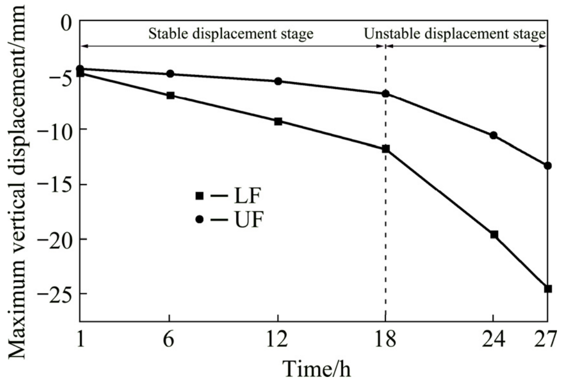

Fig. 8 Relationship between the maximum vertical displacement on two lines LF and UF and time

surfaces of Goaf U1. Especially, at the root of Pillar 6, the crack almost penetrates the entire pillar. At t=27.8 h, the lower roof suddenly sinks, resulting in the complete separation of the lower roof and the upper pillars. Then, the lower roof collapses and a chain reaction occurs upward, and severe damage happens in the upper roof and the boundary pillars, as shown in Fig. 9(e). Finally, the room-pillar model loses its bearing capacity completely, and the boundary pillars on the right are split into two pieces.

Figure 10 shows the damage characteristics of the physical model under long-term in-situ stress. It

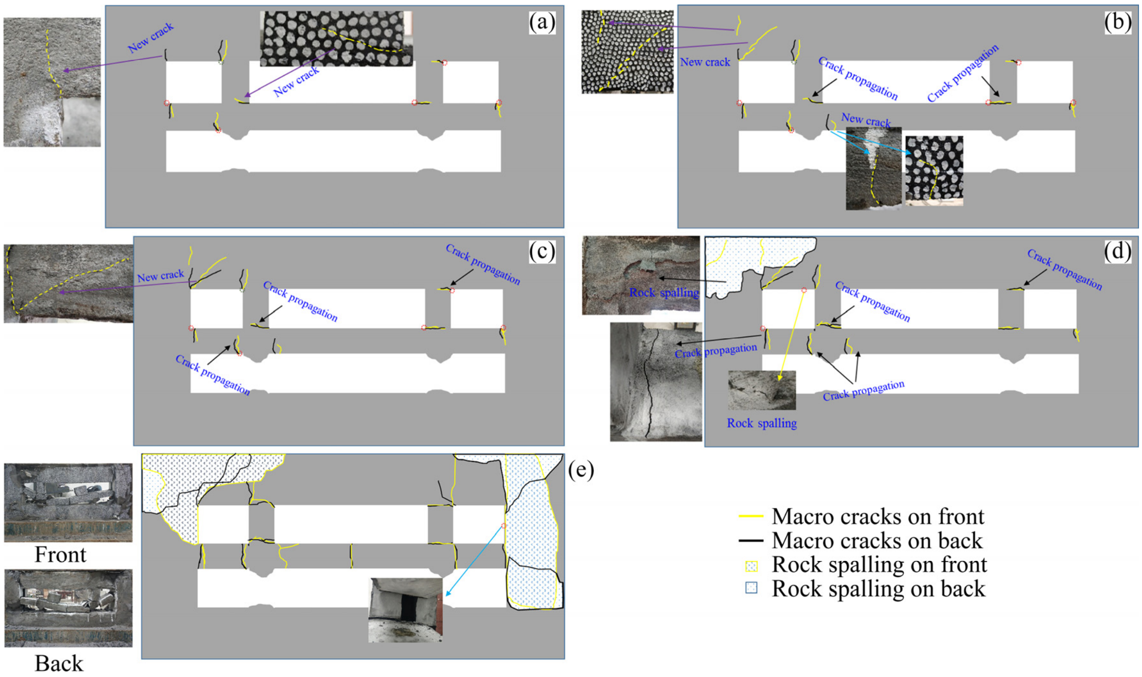

Fig. 9 Schematic diagrams of crack propagation and collapse processes of room-pillar system: (a) t=12 h; (b) t=18 h; (c) t=24 h; (d) t=27 h; (e) t=27.8 h

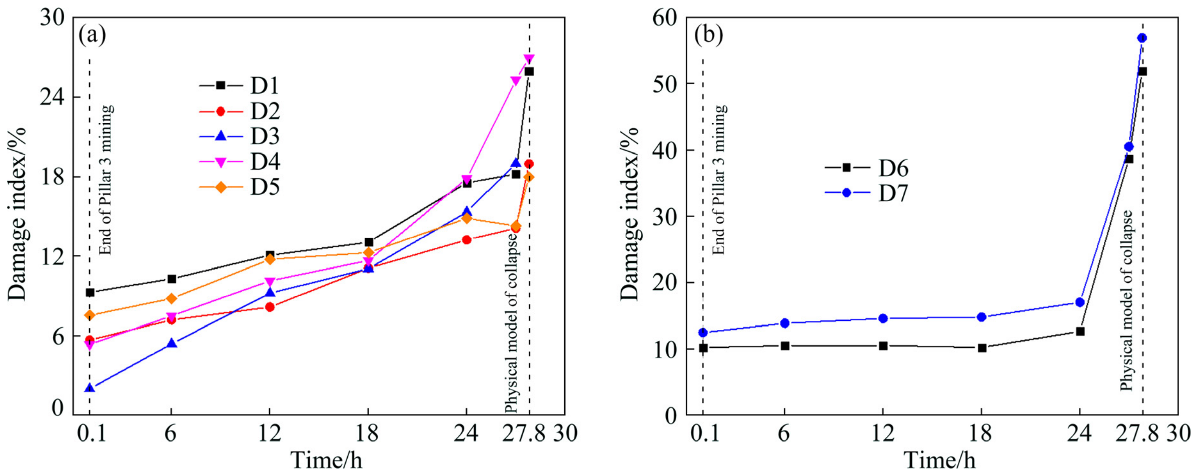

Fig. 10 Damage characteristics of physical model under long-term in-situ stress: (a) Lower roof; (b) Upper pillars

can be found that the damage in each typical area increases with time. Moreover, during 1−27.8 h, the increase of damage of the lower roof is small. The damage index of Zones D1−D5 is increased by 16.8%, 13.3%, 17%, 22% and 10.5%, respectively. Nevertheless, the increase of damage index of the upper pillars is great during 1−27.8 h, and the damage index of Zones D6 and D7 is increased by 34% and 30%, respectively. In fact, the damage characteristics of the upper pillars are closely related to the settlement process of the physical model. During 1−18 h, the physical model is in the stable displacement stage, the crack propagation and the settlement development are limited; the stress concentration in the upper pillars is not obvious, so the damage index to the upper pillar does not increase much. After t=18 h, the physical model is in the unstable displacement stage, the settlement development and crack propagation velocity increase, which causes that the loads on the upper pillars mainly concentrate in the local area. Therefore, the micro cracks in the upper pillars increase greatly, and the damage index of Zones D6 and D7 increases sharply.

6 Discussion

It is known that there are two main types of dynamic disturbances during the pillar recovery: blasting disturbance and unloading disturbance. The blasting disturbance is mainly due to the stress wave generated in the blasting process, which will cause instantaneous deformation and damage in the areas of the stress wave pathway. The unloading disturbance is mainly caused by the rapid release and transfer of the overburden loads during the pillar recovery. In fact, the surrounding rock is subjected to the combined effects of blasting disturbance and unloading disturbance during the pillar recovery. It should be noted that the effects of blasting disturbance and unloading disturbance are different. Firstly, because the unloading disturbance is mainly caused by the adjustment of the static stress in the surrounding rock [42,43], the effect of unloading disturbance will take a longer time than that of the blasting disturbance. Secondly, the blasting disturbance usually propagates in the form of stress wave [44−46], which will cause rapid deformation of the surrounding rock. The strain rate of the blasting disturbance is usually greater than that of the unloading disturbance. In addition, the strain caused by blasting disturbance will be restored to a certain extent, especially in the elastic deformation area where the deformation will be completely restored.

Assuming that the dynamic response in the surrounding rock caused by the blasting disturbance and the unloading disturbance can be represented by function $\sigma(t)$ and function $\phi(t)$, respectively. The total dynamic responses in surrounding rock can be regarded as the sum of them, that is, $\delta(t)=\sigma(t)+\phi(t)$. Figure 11 shows the dynamic response mechanism of surrounding rock during the pillar recovery. It can be found that the variation of total dynamic disturbance can be divided into three types: (I) the combined action of blasting disturbance and unloading disturbance, (II) the sequential action of blasting disturbance and unloading disturbance, and (III) the action of unloading disturbance. The characteristics of these three kinds of dynamic disturbances are described in detail as follows.

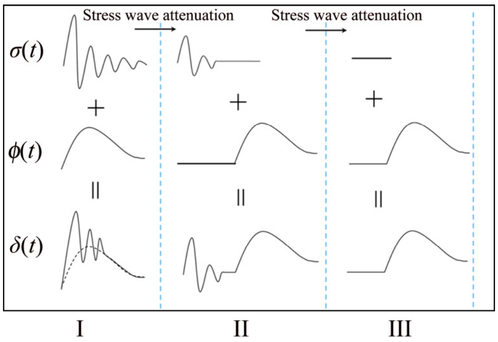

Fig. 11 Schematic diagrams of dynamic response mechanism

(I) For some areas, the action process of stress wave is usually the adjustment process of static stress in the model, so the blasting disturbance action is usually superimposed with the unloading disturbance action. In these areas, the stress−time curve and strain−time curve usually have the following characteristics: the curves usually undergo a large change, and several sharply changing peaks will be superimposed on this large trend. After going through these peaks, the curves will change gently again, as shown in Fig. 11.

(II) For some areas, the stress or strain caused by the unloading disturbance is very small or even negligible compared with that caused by the blasting disturbance, but when the blasting disturbance is over, the unloading disturbance will further cause greater stress change and strain change. For these cases, it can be considered that the processes of blasting disturbance and unloading disturbance are not overlapped, and they occur respectively according to the time sequence. In these areas, there are two distinct stages of the stress−time curve and strain−time curve. In the first stage, there are sharply changing peaks. In the second stage, the curves change gently. Furthermore, there is an obvious transition period between the two stages, as shown in Fig. 11.

(III) For some areas, due to the continuous attenuation of stress wave, the stress change caused by the blasting disturbance is almost negligible compared with the stress change caused by the unloading disturbance. Therefore, it can be considered that there are only unloading disturbances in these areas. For these regions, the stress−time curve and strain−time curve usually have no obvious sharply changing peaks, and the overall changes of these curves are gentle, as shown in Fig. 11.

In order to better evaluate the dynamic response characteristics of the room-pillar system, the strain−time curves of 10 typical monitoring points were analyzed. The distribution of these 10 typical monitoring points is shown in Fig. 12. Five monitoring points are arranged on the lower roof, named LF1, LF2, LF3, LF4 and LF5, respectively. The other five strain monitoring points are arranged on the upper roof, named UF1, UF2, UF3, UF4 and UF5, respectively. It should be noted that since the monitoring points LF3 and UF3 are in Zones ZOI1 and ZOI2, the strain−time curves of these two points will be recorded by the two high-speed cameras.

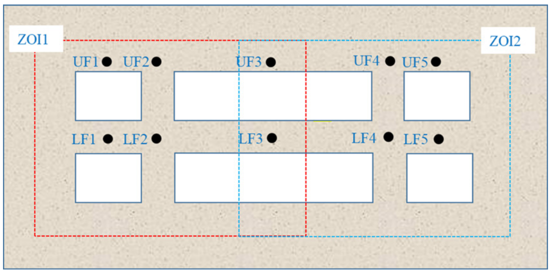

Fig. 12 Distribution of typical monitoring points

Figures 13 and 14 show the strain−time curves of the monitoring points LF and UF during Pillar 2 recovery, respectively. As shown in Fig. 13(b), LF3 (ZOI1) and LF3 (ZOI2) represent the deformation of monitoring point LF3 which is recorded by the high-speed camera 1 and high-speed camera 2, respectively. It can be found that the strain−time curves of LF3 (ZOI1) and LF3 (ZOI2) agree well, indicating that the results of the high-speed camera 1 and high-speed camera 2 are reliable. As analyzed in our previous article [33], the corresponding dynamic deformation generated by the black

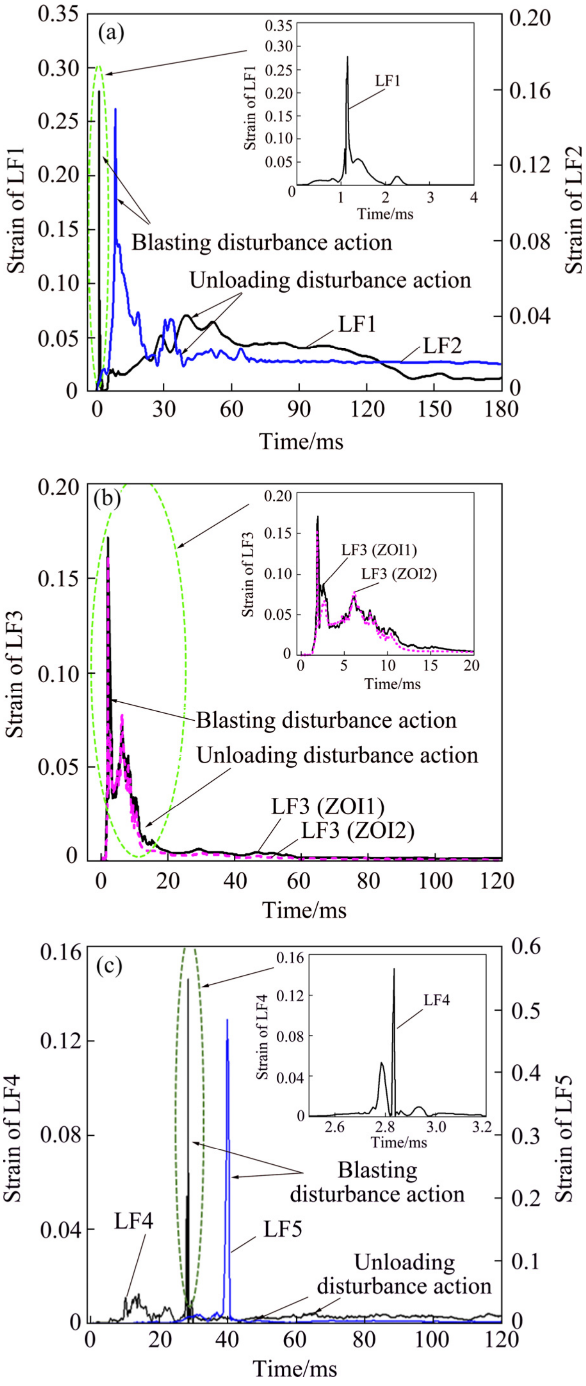

Fig. 13 Strain−time curves of monitoring points in lower roof during Pillar 2 recovery: (a) LF1 and LF2; (b) LF3; (c) LF4 and LF5

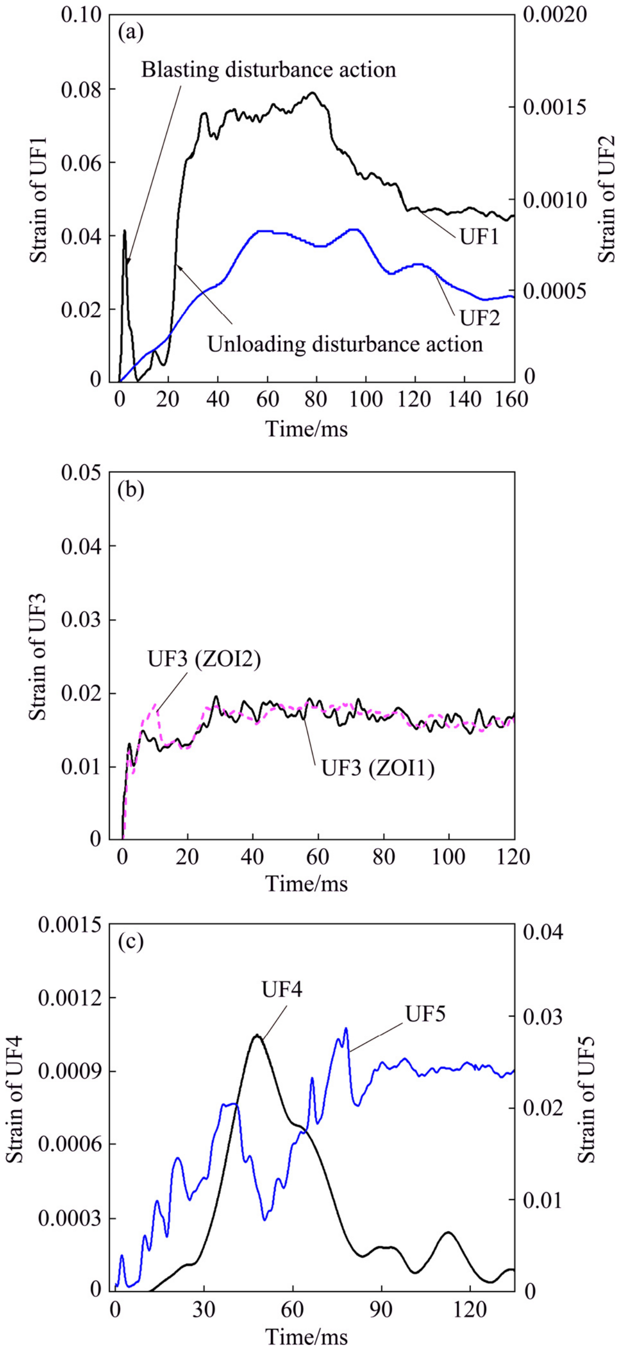

Fig. 14 Strain−time curves of monitoring points in upper roof during Pillar 2 recovery: (a) UF1 and UF2; (b) UF3; (c) UF4 and UF5

powder blasting lasts for thousands of microseconds although it is delayed due to the dynamic effect. However, most of the dynamic deformation in this study lasts for tens of thousands of microseconds or even hundreds of thousands of microseconds because the strain period is prolonged mainly by the unloading disturbance. As shown in Fig. 13, there are many sharply changing peaks in the curves. These peaks generally last for a very short time and vary dramatically, which is mainly caused by the blasting disturbances. As shown in Figs. 13 and 14, the main action processes of blasting disturbance and unloading disturbance have been identified.

As shown in Fig. 13, the strain−time curves of monitoring points LF1, LF2, LF3, LF4, and LF5 form a large peak in a very short time, and then rapidly decrease and finally stabilize after tens of thousands or even hundreds of thousands of microseconds, indicating that all these monitoring points are subjected to the I-type dynamic disturbances. As shown in Fig. 14, the strain−time curve of monitoring point UF1 increases rapidly at first and forms a large peak, and then decreases rapidly. After about 12 ms, the change of the second stage occurs. Obviously, the first strain stage is mainly caused by the blasting disturbance, and the second strain stage is mainly caused by unloading disturbance. Therefore, it can be determined that the monitoring point UF1 is subjected to the II-type dynamic disturbance. The strain−time curves of monitoring points UF2−UF5 are gentle and there are no obvious sharply changing peaks, indicating that the strains of UF2−UF5 are mainly caused by the unloading disturbances. Therefore, it can be determined that the monitoring points UF2−UF5 are subjected to the III-type dynamic disturbance.

Figures 15 and 16 show the strain−time curves of the monitoring points during Pillar 3 recovery. As shown in Figs. 15(a) and (b), there are no sharply changing peaks in the curves of monitoring points LF1−LF3, and these curves vary gently. Therefore, the monitoring points of LF1−LF3 are subjected to the III-type dynamic disturbance. As shown in Fig. 15(c), there are multiple sharply changing peaks in the curves, which are mainly caused by the blasting disturbance. Accordingly, the monitoring points LF4 and LF5 are subjected to the I-type dynamic disturbance. Similarly, it can be inferred from Fig. 16 that monitoring points of UF1−UF3 are subjected to the III-type dynamic disturbance, and the monitoring points UF4 and UF5 are subjected to the I-type dynamic disturbance.

In general, when Pillar 2 is recovered, most areas in the lower roof will be deformed under the combined action of blasting disturbance and unloading disturbance. However, in the upper roof,

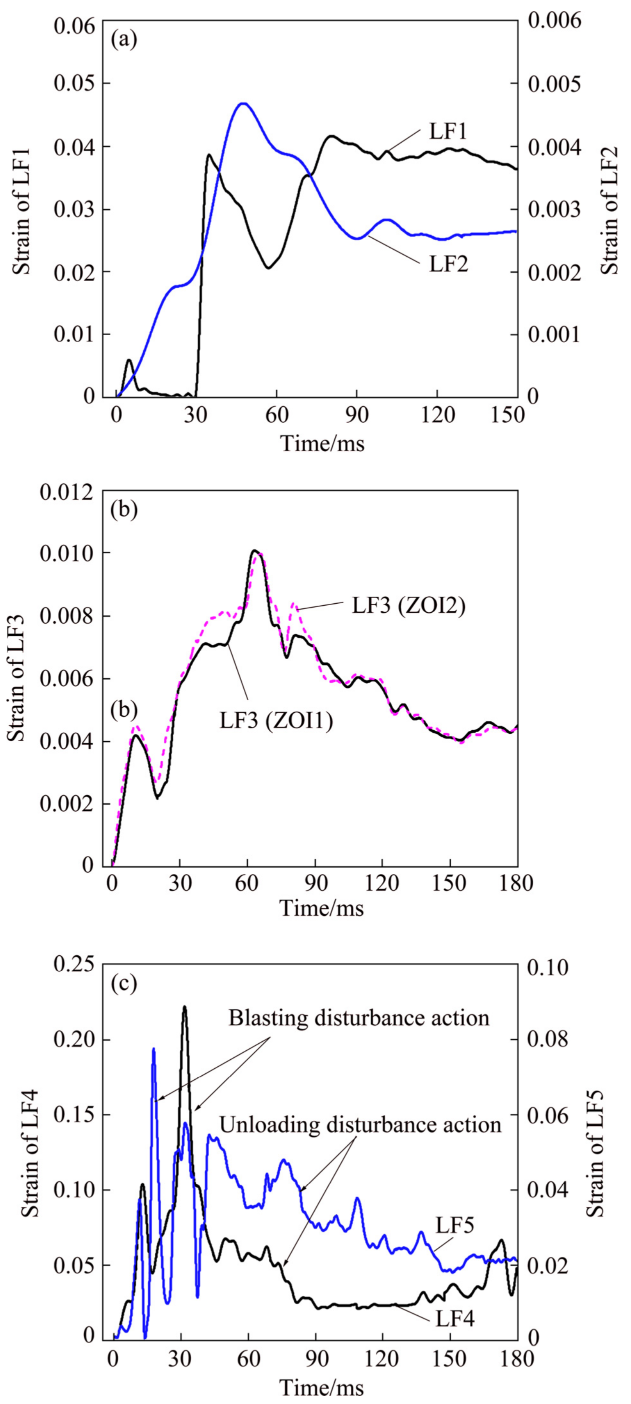

Fig. 15 Strain−time curves of monitoring points in lower roof during Pillar 3 recovery: (a) LF1 and LF2; (b) LF3; (c) LF4 and LF5

the effect of the blasting disturbance will be weakened, and the deformation is mainly caused by the unloading disturbance. When Pillar 3 is recovered, the areas near Pillar 3 will be deformed under the combined action of blasting disturbance and unloading disturbance. In the areas which are far away from Pillar 3, the deformation is mainly caused by the unloading disturbance.

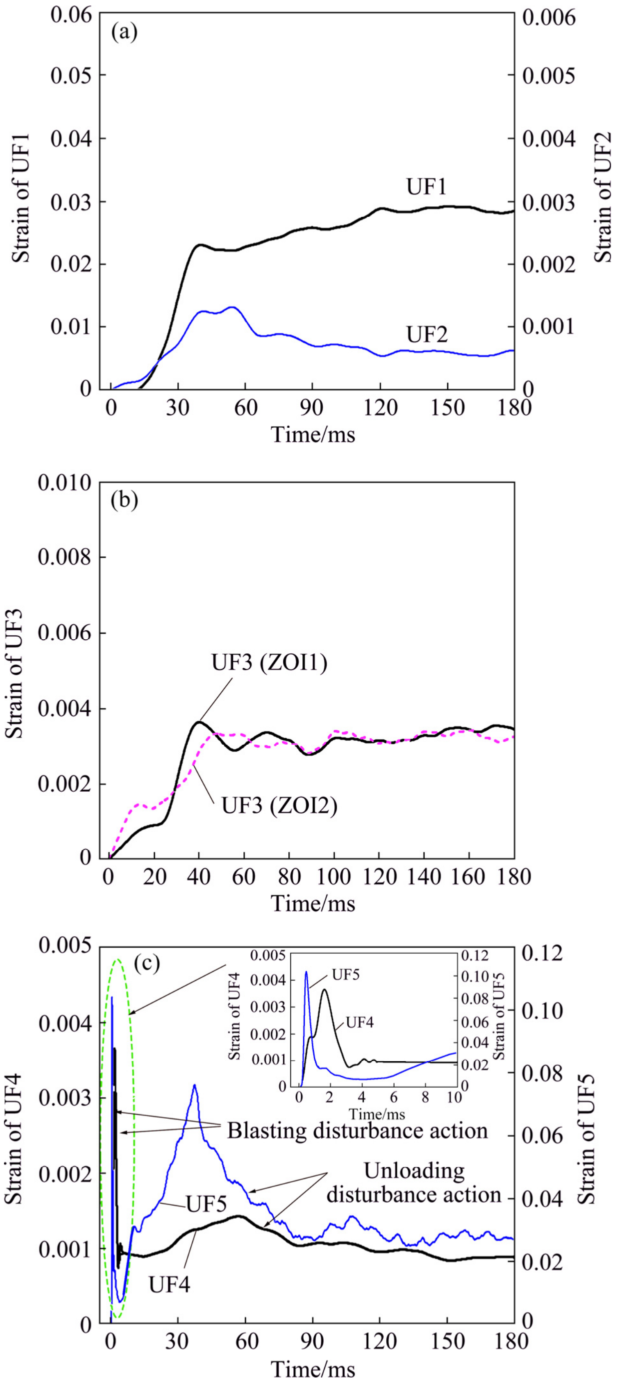

Fig. 16 Strain−time curves of monitoring points in upper roof during Pillar 3 recovery: (a) UF1 and UF2; (b) UF3; (c) UF4 and UF5

7 Conclusions

(1) During the pillar recovery, the strain mainly propagates along the edge of the lower roof to the upper level, and there will be obvious diffraction phenomena in some areas. Moreover, it is also easy to form the strain growth band between the corners of lower goafs and upper goafs. After the pillars are recovered, the roofs will sink

continuously under the action of in-situ stress. The settlement above Pillar 2 is always the largest, which stimulates the development of deformation in the adjacent areas. With the increase of time, the settlement velocity of the model will gradually increase. In general, the settlement process of the model can be divided into two stages, namely, the stable displacement stage and the unstable displacement stage.

(2) During the pillar recovery, macro cracks are prone to occur at the corners of goafs. After pillar recovery, a series of new cracks will appear in the upper pillars and roofs under the long-term effect of in-situ stress. These cracks extend with the increase of roofs settlement. When the model is in the unstable displacement stage, rock spalling will occur in the goaf. When the model settlement increases to a certain extent, the lower roof will suddenly collapse and further cascading failure will occur. No matter during or after the pillar recovery, the damage of the upper pillars is usually greater than that of the lower roof.

(3) During the pillar recovery, there are two kinds of dynamic disturbances in the model, namely blasting disturbance and unloading disturbance. In different regions, the effects of these two types of disturbances are different. The total dynamic disturbances can be divided into three types: (I) the combined action of blasting disturbance and unloading disturbance, (II) the sequential action of blasting disturbance and unloading disturbance, and (III) the action of unloading disturbance. The strain−time characteristics of typical regions have also been further analyzed. The results show that when Pillar 2 is recovered, the lower roof is mainly subjected to I-type dynamic disturbance, the upper roof is mainly subjected to III-type dynamic disturbance, and a few areas are affected by II-type dynamic disturbance. When Pillar 3 is recovered, the areas near Pillar 3 are mainly subjected to I-type dynamic disturbance, and the areas far from Pillar 3 are mainly subjected to III-type dynamic disturbance.

References

[1] MARTIN C D, MAYBEE W G. The strength of hard-rock pillars [J]. International Journal of Rock Mechanics and Mining Sciences, 2000, 37: 1239−1246.

[2] KAISER P K, KIM B H, BEWICK R P, VALLEY B. Rock mass strength at depth and implications for pillar design [J]. Mining Technology, 2014, 120: 170−179.

[3] GUO W B, HOU Q L, ZOU Y F. Relationship between surface subsidence factor and mining depth of strip pillar mining [J]. Transactions of Nonferrous Metals Society of China, 2011, 21: s594−s598.

[4] GUO W B, XU F Y. Numerical simulation of overburden and surface movements for Wongawilli strip pillar mining [J]. International Journal of Mining Science and Technology, 2016, 26: 71−76.

[5] CHEN S J, GUO W J, ZHOU H, WEN G H. Structure model and movement law of overburden during strip pillar mining backfill with cream-body [J]. Journal of China Coal Society, 2011, 36: 1081−1086. (in Chinese)

[6] HAUQUIN T, DECK O, GUNZBERGER Y. Average vertical stress on irregular elastic pillars estimated by a function of the relative ratio [J]. International Journal of Rock Mechanics and Mining Sciences, 2016, 83: 122−134.

[7] CHEN Y, MA S Q, YU Y. Stability control of underground roadways subjected to stresses caused by extraction of a 10-m-thick coal seam: a case study [J]. Rock Mechanics and Rock Engineering, 2017, 50: 2511−2520.

[8] ZHANG G C, HE F L, JIA H G, LAI Y H. Analysis of gateroad stability in relation to yield pillar size: A case study [J]. Rock Mechanics and Rock Engineering, 2017, 50: 1263−1278.

[9] BRADY B, BROWN E. Rock mechanics: For underground mining [M]. New York: Springer, 2013.

[10] JAWED M, SINHA R K, SENGUPTA S. Chronological development in coal pillar design for bord and pillar workings: a critical appraisal [J]. Journal of Geology and Mining Research, 2013, 5: 1−11.

[11] POULSEN B A. Coal pillar load calculation by pressure arch theory and near feld extraction ratio [J]. International Journal of Rock Mechanics and Mining Sciences, 2010, 47: 1158−1165.

[12] POULSEN B A, SHEN B. Subsidence risk assessment of decommissioned bord-and-pillar collieries [J]. International Journal of Rock Mechanics and Mining Sciences, 2013, 60: 312−320.

[13] ESTERHUIZEN G S, DONLINAR D R, ELLENBERGER J L. Pillar strength in underground stone mines in the united states [J]. International Journal of Rock Mechanics and Mining Sciences, 2011, 48: 42−50.

[14] LUNDER P, PAKALNIS R. Determination of the strength of hard-rock mine pillars [J]. CIM Bulletin, 1997, 90: 51−55.

[15] ZHOU Z L, CHEN L, CAI X, SHEN B T, ZHOU J, DU K. Experimental investigation of the progressive failure of multiple pillar-roof system [J]. Rock Mechanics and Rock Engineering, 2018, 51: 1629−1636.

[16] ZHOU Z L, ZHAO Y, CAO W Z, CHEN L, ZHOU J. Dynamic response of pillar workings induced by sudden pillar recovery [J]. Rock Mechanics and Rock Engineering, 2018, 51: 3075−3090.

[17] ZHU W B, CHEN L, ZHOU Z L, SHEN B T, XU Y. Failure propagation of pillars and roof in a room and pillar mine induced by longwall mining in the lower seam [J]. Rock Mechanics and Rock Engineering, 2019, 52: 1193−1209.

[18] FANG Z, HARRISON J P. Numerical analysis of progressive fracture and associated behaviour of mine pillars by use of a local degradation model [J]. Mining Technology, 2002, 111: 59−72.

[19] AL HEIB M, DUVAL C, THEOLEYER F, JEAN MARC W, PHILIPPE G. Analysis of the historical collapse of an abandoned underground chalk mine in 1961 in Clamart (Paris, France) [J]. Bulletin of Engineering Geology and the Environment, 2015, 74: 1001−1018.

[20] ZHU D F, TU S H. Mechanisms of support failure induced by repeated mining under gobs created by two-seam room mining and prevention measures [J]. Engineering Failure Analysis, 2017, 82: 161−178.

[21] ZHU W B, XU J M, LI Y C. Mechanism of the dynamic pressure caused by the instability of upper chamber coal pillars in Shendong coalfield, China [J]. Geosciences Journal, 2017, 21: 729−741.

[22] CORDING E J, HASHASH Y M A, OH J. Analysis of pillar stability of mined gas storage caverns in shale formations [J]. Engineering Geology, 2015, 184: 71−80.

[23] ZIPF R K J. Simulation of cascading pillar failure in room-and pillar mines using boundary-element method [C]// Proceedings of the 2nd North American Rock Mechanics Symposium. American Rock Mechanics Association. Montreal, Canada, 1996: 1887−1892.

[24] LI X B, GONG F Q, TAO M, DONG L J, DU K, MA C D, ZHOU Z L, YIN T B. Failure mechanism and coupled static-dynamic loading theory in deep hard rock mining: A review [J]. Journal of Rock Mechanics and Geotechnical Engineering, 2017, 9: 767−782.

[25] QIU J D, LI D Y, LI X B, ZHU Q Q. Numerical investigation on the stress evolution and failure behavior for deep roadway under blasting disturbance [J]. Soil Dynamics and Earthquake Engineering, 2020, 137: 106278.

[26] ZHOU T, ZHU J B, XIE H P. Mechanical and volumetric fracturing behaviour of three-dimensional printing rock-like samples under dynamic loading [J]. Rock Mechanics and Rock Engineering, 2020, 53: 2855−2864.

[27] WANG S L, HAO S P, CHEN Y, BAI J B, WANG X Y, XU Y. Numerical investigation of coal pillar failure under simultaneous static and dynamic loading [J]. International Journal of Rock Mechanics and Mining Sciences, 2016, 84: 59−68.

[28] LI X B, LI D Y, GUO L, YE Z Y. Study on mechanical response of highly-stressed pillars in deep mining under dynamic disturbance [J]. Chinese Journal of Rock Mechanics and Engineering, 2007, 26: 922−928. (in Chinese)

[29] CAI M F, LIU W D, LI Y. In-situ stress measurement at deep position of Linglong Gold Mine and distribution law of in-situ stress field in mine area [J]. Chinese Journal of Rock Mechanics and Engineering, 2010, 29: 227−233. (in Chinese)

[30] ZHU Q Q, LI D Y, HAN Z Y, LI X B, ZHOU Z L. Mechanical properties and fracture evolution of sandstone specimens containing different inclusions under uniaxial compression [J]. International Journal of Rock Mechanics and Mining Sciences, 2019, 115: 33−47.

[31] WENG L, WU Z J, LIU Q S. Influence of heating/cooling cycles on the micro/macrocracking characteristics of Rucheng granite under unconfined compression [J]. Bulletin of Engineering Geology and the Environment, 2020, 79: 1289−1309.

[32] WU Q H, CHEN L, SHEN B T, DLAMINI B, LI S Q, ZHU Y J. Experimental investigation on rockbolt performance under the tension load [J]. Rock Mechanics and Rock Engineering, 2019, 52: 4605−4618.

[33] QIU J D, LI X B, LI D Y, ZHAO Y Z, HU C W, LIANG L S. Physical model test on the deformation behavior of an underground tunnel under blasting disturbance [J]. Rock Mechanics and Rock Engineering, 2020. https://doi.org/10.1007/s00603-020-02249-2

[34] LI X H. Simulation experiment technique of rock mechanics [M]. Beijing: Science Press, 2007. (in Chinese)

[35] SU C D, QIU J D, WU Q H, WENG L. Effects of high temperature on the microstructure and mechanical behavior of hard coal [J]. International Journal of Mining Science and Technology, 2020, 30: 643−650

[36] LIU K, LI Q Y, WU C Q, LI X B, LI J. Optimization of spherical cartridge blasting mode in one-step raise excavation using pre-split blasting[J]. International Journal of Rock Mechanics and Mining Sciences, 2020, 126: 104182.

[37] WANG F, CAO P, WANG Y X, HAO R Q, MENG J J, SHANG J L. Combined effects of cyclic load and temperature fluctuation on the mechanical behavior of porous sandstones [J]. Engineering Geology, 2020, 266: 105466.

[38] WANG J A, LI D Z, SHANG X C. Creep failure of roof stratum above mined-out area [J]. Rock Mechanics and Rock Engineering, 2012, 45: 533−546.

[39] BISWAS K, MARK C, PENG S S. A unique approach to determining the time-dependent in situ strength of coal pillars [C]//Proceedings of the Second International Workshop on Coal Pillar Mechanics and Design. Pittsburgh, PA: Department of Health and Human Services. 1999: 5−13.

[40] MALAN D F. Simulating the time-dependent behaviour of excavations in hard rock [J]. Rock Mechanics and Rock Engineering, 2002, 35: 225−254.

[41] QIU J D, LUO L, LI X B, LI D Y, CHEN Y, LUO Y. Numerical investigation on the tensile fracturing behavior of rock-shotcrete interface based on discrete element method [J]. International Journal of Mining Science and Technology, 2020, 30: 293−301.

[42] CHEN Z H, LI X B, DUSSEAULT M B, WENG L. Effect of excavation stress condition on hydraulic fracture behaviour [J]. Engineering Fracture Mechanics, 2020, 226: 106871.

[43] LI X B, CHEN Z H, WENG L, LI C J. Unloading responses of pre-flawed rock specimens under different unloading rates [J]. Transactions of Nonferrous Metals Society of China, 2019, 29: 1516−1526.

[44] WU Q H, LI X B, WENG L, LI Q F, ZHU Y J, LUO R. Experimental investigation of the dynamic response of

prestressed rockbolt by using an SHPB-based rockbolt test system [J]. Tunnelling and Underground Space Technology, 2019, 93: 103088.

[45] LIU K, WU C Q, LI X B, LI Q Y, FANG J G, LIU J. A modified HJC model for improved dynamic response of brittle materials under blasting loads [J]. Computers and Geotechnics, 2020, 123: 103584.

[46] LI Q Y, LIU K, LI X B, WANG Z W, WENG L. Cutting parameter optimization for one-step shaft excavation technique based on parallel cutting method [J]. Transactions of Nonferrous Metals Society of China, 2018, 28: 1413−1423.

矿柱回采诱发的深部房柱系统的瞬态及长期变形特性

李夕兵[1]，邱加冬[1,2]，赵宇喆[1]，陈正红[1]，李地元[1]

1. 中南大学 资源与安全工程学院，长沙 410083；
2. 深圳大学 深圳市深部工程科学与绿色能源重点实验室，深圳 518060

摘　要：当采用房柱法开采深部矿石矿柱时，采空区可能面临着一系列的变形和沉降问题。为此，构建一个双中段的深部房柱模型并进行矿柱回采。分析矿柱回采瞬间的变形响应及矿柱回采后的长期沉降特性。在矿柱回采过程中，不同区域围岩受到不同动力扰动作用，这些动力扰动可以分为 3 类：(I) 爆破扰动与卸荷扰动共同作用、(II) 爆破扰动与卸荷扰动依序作用和(III)纯卸荷扰动作用。矿柱回采后，第一个回采矿柱上方的沉降最大，且它对周边区域的沉降起到牵引作用。模型的沉降过程可分为稳定位移及不稳定位移两个阶段。当房柱系统进入不稳定位移阶段时，将发生岩体剥落及级联式坍塌。

关键词：房柱系统；物理模型测试；沉降；动态响应；变形

(Edited by Wei-ping CHEN)